npj | flexible electronics

Article

Published in partnership with Nanjing Tech University

https://doi.org/10.1038/s41528-026-00574-0

Bioabsorbable Si-Mg galvanic cells in flexible scaffolds for symbiotic electrical stimulation to promote nerve regeneration

Engui Wang[1,2,8], Jing Huang[1,8], Yizhu Shan[3,8], Lin Luo[1], Yongfang Ren[1], Xiaozhou Wen[1], Yichang Quan[1], Chang Zhu[1], Xu Wu[1], Xi Cui[2,4], Yuan Bai[5], Dongjie Jiang[5], Bojing Shi[6], Xia Wang[7], Hongqing Feng[1] ✉, Lingling Xu[1] ✉, Zhou Li[2,4] ✉ & Han Ouyang[1] ✉

Electrical stimulation treatment represents a new paradigm for tissue regeneration and reconnection. However, the deployment of electrical stimulation devices on damaged and dynamic tissues in vivo remains challenging. Here, we present transient Si–Mg galvanic cell scaffolds for symbiotic electrical stimulation scaffolds (SESS), where tissue fluids act as the electrolyte to drive the galvanic reaction, enabling month-long nonlinear and adaptive electrical stimulation for enhancing nerve regeneration and reconnection. The SESS integrates all biodegradable materials into a seamless textile, enabling deployment on dynamic tissues and full degradation that eliminates the need for secondary removal surgery. Owing to the suitable impedance and biocompatibility of the semiconductor silicon-biological interface, SESS can generate up to month long effective electrical output. SESS showed therapeutic efficacy comparable to autologous nerve grafts in a 10-mm rat sciatic nerve defect model. Notably, the therapeutic effects from degradation products and electrical stimulation have been decoupled and determined via mirror-symmetric deployment. This work should provide new insights and pathways for the development of galvanic cell bioelectronics.

Electrical stimulation therapy is empowering tissue regeneration implants to deliver better wound management, spinal cord and nerve repair, heart failure treatment[1–9]. However, deploying electrical stimulation implants on dynamically damaged tissues and achieving stable, controllable energy supply remains challenging[10–14]. At present, Electrical stimulation tissue regeneration implants can utilize triboelectric[5,15,16], piezoelectric[3,17–19], and RF (radio frequency) wireless[20–23] power to mimic endogenous electrical fields and guide tissue regeneration and reconnection[2,4,24–26]. Triboelectric and piezoelectric scaffolds generate signals via mechanical deformation or body motion, but their output is unstable and transient, and they typically rely on dynamic activation. Wireless power transfer systems enable programmable external stimulation via electromagnetic coupling, yet their bulky design, structural complexity, and reliance on external transmitting sources result in reduced patient compliance.

Recently reported biofluid-driven self-powered scaffolds eliminate the need for external power by using the spontaneous electrochemical reactions of electrode materials in body fluids to generate current for stimulation (Table S1)[6,27–29]. However, they remain limited by the rapid consumption of active metal electrodes and the suboptimal degradation or degradation products of certain materials, which may cause potential chronic inflammation and side effects. Prolonged controllable operation and complete degradation remain unmet requirements for self-powered tissue regeneration implants to advance toward clinical application. It remains unclear whether therapeutic effects stem from electrical stimulation or from the degradation products of the device, due to the generation of electrical

---

[1]School of Nanoscience and Engineering, College of Materials Science and Opto-Electronic Technology, University of Chinese Academy of Sciences, Beijing, 100049, China. [2]Vita Tech Innovation Center, Tsinghua Changgung Hospital, School of Clinical Medicine, Tsinghua University, Beijing, 100084, China. [3]Institute of Forensic Science of Tianjin Public Security, Tianjin, 300384, China. [4]School of Biomedical Engineering, Tsinghua Medicine, Tsinghua University, Beijing, 100084, China. [5]Department of Advanced Manufacturing and Robotics, College of Engineering, Peking University, Beijing, 100871, China. [6]Key Laboratory for Biomechanics and Mechanobiology of Chinese Education Ministry, Beijing Advanced Innovation Centre for Biomedical Engineering, School of Biological Science and Medical Engineering, Beihang University, Beijing, 100191, China. [7]The Key Laboratory of Land Resources Evaluation and Monitoring in Southwest China, College of Geography and Resources, Sichuan Normal University, Chengdu, 610066, China. [8]These authors jointly supervised this work: Engui Wang, Jing Huang, Yizhu Shan ✉e-mail: fenghongqing@ucas.ac.cn; xulingling@ucas.ac.cn; li_zhou@tsinghua.edu.cn; ouyanghan@ucas.ac.cn

stimulation and the degradation products occurring synchronously and being closely associated.

In the context of validating the regenerative capacity of therapeutic interventions, peripheral nerve injury (PNI) models emerge as the optimal candidates. A key consideration is that peripheral nerves exhibit distinct responses to different directions of electrical stimulation. This property facilitates the decoupling of device degradation products from the effects of electrical stimulation on tissue regeneration and repair via mirror-symmetric deployment of the device. In addition, peripheral nerves, particularly the sciatic nerve, exhibit significant dynamic properties, providing an optimal platform for validating the deployment capabilities of electrical stimulation implants on dynamic tissues. Finally, the challenging and widespread nature of peripheral nerve injury is an important consideration. Millions of patients worldwide are suffering from severe PNI, which is a growing global challenge. Following suboptimal treatment, PNI patients are often accompanied by sensory loss, motor dysfunction, and muscle atrophy, which severely compromising patients and their family quality of life[1,30–36].

Here, we present transient Si–Mg galvanic cell scaffolds for symbiotic electrical stimulation scaffolds (SESS), where tissue fluids drive the galvanic reaction to generate month-long nonlinear and adaptive electrical stimulation while consuming reactive oxygen species (ROS). The SESS consists entirely of biodegradable components, including a PCL/Mg electrochemically active layer and Mo/Si electrodes assembled onto the soft aligned PCL fibrous matrix. The unidirectional conduction of nerves is mimicked by SESS that generating directed currents to promote axonal regeneration while releasing Mg^{2+} to aid Schwann cell proliferation and myelination[37–40]. In a 10-mm rat sciatic nerve defect model, SESS showed favorable therapeutic efficacy equivalent to autologous nerve grafts while completely degrading in vivo, eliminating the need for secondary surgery. The therapeutic effects of electrical output have been determined systematically via mirror-symmetric deployment. This work introduces a galvanic cell bioelectronics strategy to produce electrical stimulation for tissue regeneration and reconnection.

Results

Design of SESS

The concept and functional design of the SESS for promoting peripheral nerve repair, such as after sciatic nerve injury, are illustrated in Fig. 1a. The device interfaces directly with the injured site, bridging the nerve gap and providing directed electrical stimulation to promote axonal regeneration and neuromuscular reinnervation of the lateral gastrocnemius muscle.

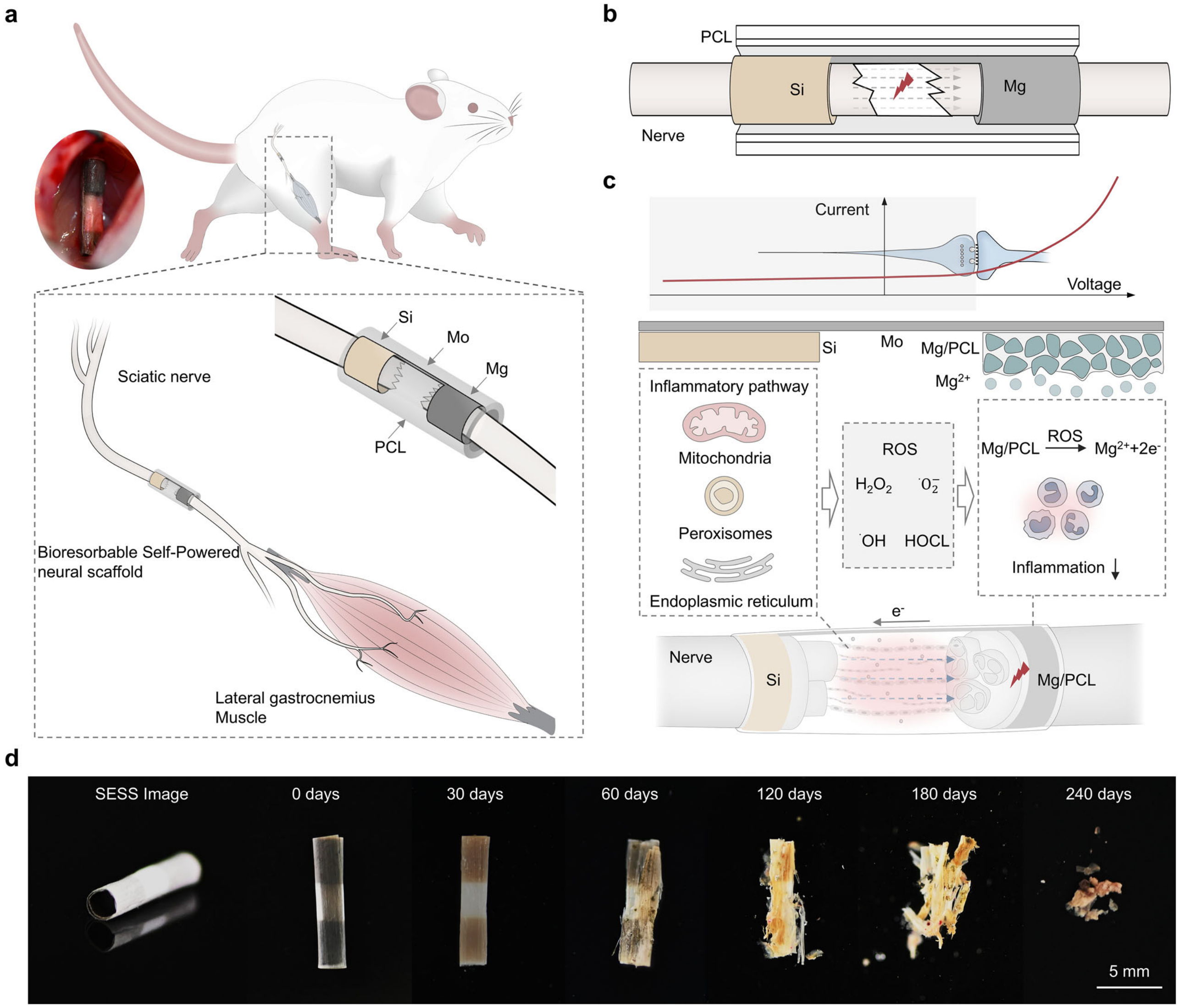

Fig. 1 | SESS for nerve repair. a Schematic illustration of SESS implantation in the animal model. **b** Structural schematic of the SESS. **c** Illustration of SESS consuming reactive oxygen species from pathological interstitial fluid to generate electrical stimulation for nerve repair. **d** Photographs showing the accelerated degradation of SESS in vitro (PBS, 60 °C).

Structurally, the SESS consists of three primary components (Fig. 1b): (i) a substrate formed by aligned PCL fibers, which provides both physical support and directional guidance for axonal regeneration; (ii) an electrochemically active PCL/Mg layer interacts with interstitial fluid at the lesion site, triggering controlled electrochemical reactions that release Mg^{2+} and scavenge excessive ROS. This ROS elimination reduces oxidative stress and inflammation, thereby preserving Schwann cell activity and promoting axonal growth and nerve regeneration; and (iii) a composite structure integrating molybdenum electrodes with a silicon semiconductor layer, designed to ensure stable electronic transmission and to optimize the electrode–tissue interface for reliable signal delivery.

The SESS employs a diode-like configuration that ensures unidirectional current flow, mimicking natural nerve signaling. At the same time, the Mg-based electrode interacts with pathological tissue fluid, undergoing controlled electrochemical reactions that consume ROS such as H_2O_2, $O_2\bullet^-$, and •OH. This process reduces local oxidative stress and inflammatory responses, while simultaneously establishing a pro-regenerative microenvironment. Through the combined effects of electrical guidance and biochemical modulation, the SESS accelerates neural repair (Fig.1c). In addition, the device exhibits gradual degradation over 240 days, during which its structural components slowly disappear through hydrolysis, leaving only a few small fragments at the end (Fig.1d). These residual fragments are expected to continue degrading over a longer period until complete disappearance. This fully bioresorbable property eliminates the need for secondary surgical removal, ensuring a safe and patient-friendly therapeutic approach.

Physical and electrical characterization of SESS

SESS was fabricated through a multistep process that combines polymer electrospinning and metal/semiconductor deposition (Fig. 2a, Fig. S1). First, aligned PCL fibers were produced by electrospinning to form a porous and flexible substrate. Subsequently, Mo, Mg, and Si layers were sequentially deposited via magnetron sputtering. These functional layers not only enable electrical rectification and stable signal transmission but also undergo controlled hydrolytic degradation, with Mg and Si converting into biocompatible hydroxides, thereby ensuring the device's eventual resorption in vivo.

The resulting PCL exhibits excellent flexibility and mechanical compliance, as shown in Fig. 2b, where it can be bent and twisted without fracture, demonstrating its suitability for integration with soft peripheral nerve tissue. Elemental mapping further confirms the uniform distribution of Mo, Mg, and Si on the PCL substrate (Fig. 2c), validating the precise structural design. Mechanical testing indicates that the SESS can sustain strains approaching 1000% while maintaining tensile stability (Fig. 2d), a critical feature for conformal contact with dynamic biological environments.

In addition to its mechanical robustness, the SESS maintains favorable physiological properties. Water vapor transmission rate (WVTR) and water retention measurements demonstrated that the scaffold possessed appropriate breathability comparable to that of medical gauze and pristine PCL, which facilitates gaseous and nutrient exchange while maintaining a moist environment conducive to nerve regeneration (Fig. S2). Moreover, the scaffold provides a high specific surface area, which enhances its capacity for axonal adhesion and growth, further supporting functional recovery.

To evaluate the SESS's capability of utilizing ROS, hydrogen peroxide and ferrous sulfate were used to generate ROS through the Fenton reaction. The SESS was incubated with the reaction solution for different durations, followed by the addition of methyl violet, which reacts with ROS. In the blank group, ROS generated by the Fenton reaction degraded methyl violet, resulting in a colorless solution. In contrast, when SESS was introduced, it scavenged the ROS produced by the Fenton reaction, and the color of methyl violet remained largely unchanged. The absorption spectra further confirmed that BSNS effectively consumed ROS without significantly degrading methyl violet (Fig. 2e). Eliminating ROS reduces oxidative stress and inflammation, creating a favorable environment for nerve regeneration. Additionally, ROS accelerates the electrochemical reactions at the scaffold electrodes, boosting the electrical output of SESS (Fig. S3).

Upon contact with body fluids in vivo, SESS undergoes controllable electrochemical reactions, thereby continuously generating electrical signals to provide stimulation to the target tissue and promote repair (Fig. 2f). To more directly visualize this process, Mg/PCL composites were characterized by SEM at different time points in PBS (Fig. S4). The results showed that on day 0, Mg particles were fully encapsulated by the PCL layer, effectively preventing direct contact between water and Mg and avoiding rapid Mg consumption. With prolonged immersion, cracks gradually appeared in the PCL layer, and Mg particles were progressively consumed and released electrons, driving the spontaneous electricity generation of the scaffold. This gradual degradation mode ensures that the device can provide long-term stable stimulation during the critical period of tissue repair, rather than delivering short-term bursts.

Further impedance matching tests revealed that the impedance of SESS is approximately 200 kΩ, comparable to that of injured peripheral nerve tissue (Fig. 2g, Figs. S5 and S6). This matching is crucial for nerve repair: on one hand, it minimizes interfacial energy loss and ensures efficient signal transmission; on the other hand, it enables good electrical coupling with regenerating axons, ensuring precise modulation of nerve regeneration. Moreover, SESS exhibits a maximum power output of ~0.15 μW, sufficient to meet the requirements for electrical stimulation in nerve repair. Notably, I–V characterization confirmed the diode-like behavior of SESS, exhibiting unidirectional conduction, which ensures current flows preferentially in the desired orientation for effective axonal guidance (Fig. S7). Long-term stability tests in PBS, simulating the in vivo environment, showed that the open-circuit voltage of the device decreased from an initial 400 mV to ~80 mV after 3 weeks, still within a range capable of modulating nerve regeneration (Fig. 2h)[1,41,42]. This dynamic change in electrical output ensures sufficient stimulation during the early stages of repair, while gradually decreasing to a safe level at later stages, thereby avoiding potential tissue damage or abnormal nerve excitability caused by excessive stimulation. In addition, due to the flexibility of the scaffold, its electrical performance remains stable under bending, further supporting reliable stimulation under the dynamic conditions of neural tissue (Fig. S8).

In vitro evaluation biosafety and cell behavior of SESS

Favorable biocompatibility is the fundamental requirement for implantable devices. To evaluate the biocompatibility of SESS and its potential to support nerve repair, a series of experiments was conducted. Hemocompatibility testing was performed to ensure that SESS does not induce hemolysis when in contact with blood (Fig. 3a). The hemolysis rate of SESS was comparable to the negative control and significantly lower than the positive control, indicating excellent blood compatibility. Cytocompatibility was evaluated using HaCaT cells in a CCK-8 assay, which showed high cell viability across control, PCL, and SESS groups, suggesting negligible cytotoxicity of the materials (Fig. 3b). Live/dead staining confirmed this result; cells in each group exhibited near-complete viability, with few dead cells observed (Fig. 3c).

To evaluate the potential of SESS to support neural repair, mesenchymal stem cells (MSCs), which serve as progenitor cells capable of differentiating into neural lineages, were cultured on SESS substrates. After seeding mesenchymal stem cells (MSCs) onto the SESS substrates, we observed that the cells exhibited favorable adhesion and spreading. Compared with MSCs cultured on TCP substrates, those on the SESS substrates displayed distinct alignment, indicating that the SESS structure can mimic neural tissue architecture and may facilitate peripheral nerve repair (Fig. 3d). The long-term in vivo biocompatibility of SESS was also assessed. Three months after implantation along the rat sciatic nerve, histological analysis of major organs showed no significant differences compared with the blank control group (Fig. S9), and blood routine parameters remained within normal ranges (Fig. S10), confirming the excellent biocompatibility and systemic safety of SESS. It is important to note that the materials used in the device, including PCL, Si, Mg, and Mo, have been used in FDA-approved

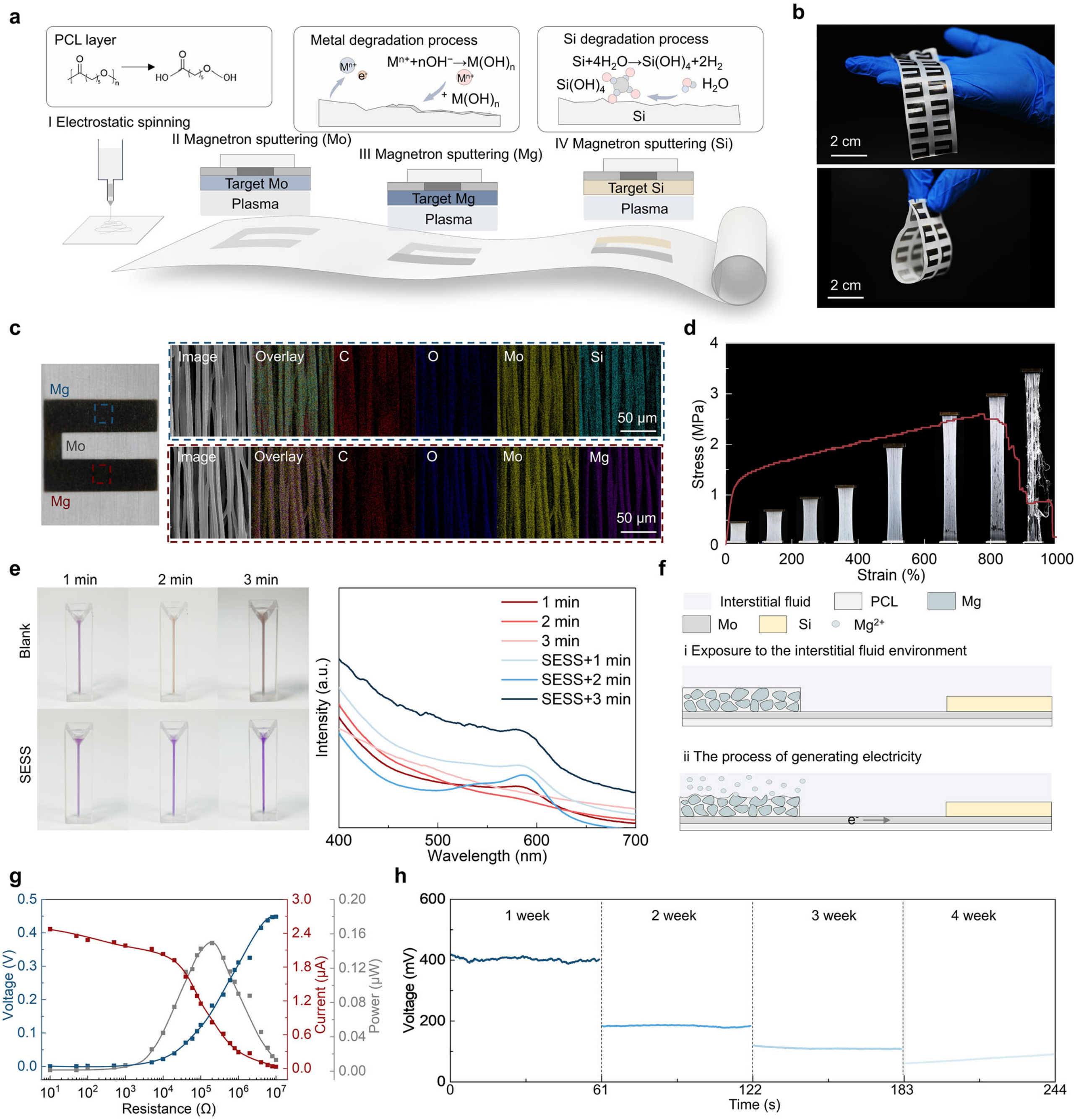

Fig. 2 | Physical and electrical properties of the SESS scaffold. **a** Schematic illustration of the fabrication process of SESS. **b** Optical image of SESS. **c** EDS spectra of different regions of SESS. **d** Stress–strain curve of the PCL material. **e** SESS consumes ROS, methyl violet degradation experiment. **f** Schematic diagram of the electricity generation mechanism of SESS. **g** Impedance spectra of SESS. **h** Long-term electrical output of SESS in PBS solution in vitro.

implantable devices, supporting the biocompatibility and clinical translational potential of the scaffold (Tables S2 and S3).

A scratch assay was performed to evaluate the effect of electrical stimulation on cell migration and repair (Fig. 3e, f). Under electrical stimulation (ES, 50 mV, direct current (DC)), the scratch area of cells (ES group) was 0.31 ± 0.03 mm^2, while the scratch area of cells without ES (Ctrl group) was 0.39 ± 0.03 mm^2. Compared to the ES group, the Ctrl group exhibited a significantly larger area. These results indicate that the weak electrical stimulation provided by SESS can effectively promote cell migration and thus has the potential to accelerate the nerve repair process.

PC12 cells, a neuronal model capable of extending axons under differentiation conditions, were used to evaluate the promoting effect of SESS on axonal elongation. The cells were seeded on TCP, PCL, and SESS substrates and cultured for 7 days, after which axonal elongation was assessed by immunofluorescence. Compared to cells on TCP, those on PCL and SESS exhibited significant directional growth. Furthermore, under electrical stimulation (50 mV, DC), PC12 cells on SESS developed longer axons than those on PCL, suggesting that the combination of SESS substrate and weak electrical cues can enhance axonal elongation (Fig. 3g, h).

To evaluate the ability of SESS to guide nerve growth at the tissue level, dorsal root ganglia (DRG) explants were cultured on SESS, and neuronal growth was assessed by immunofluorescence staining. In the TCP culture group, neurons and glial cells exhibited a network-like growth pattern, whereas axons extending from DRG explants in the PCL and SESS groups exhibited directional growth, with those on SESS being longer than on PCL (Fig. 3i, j). Taken together, these results indicate that the ordered micro/

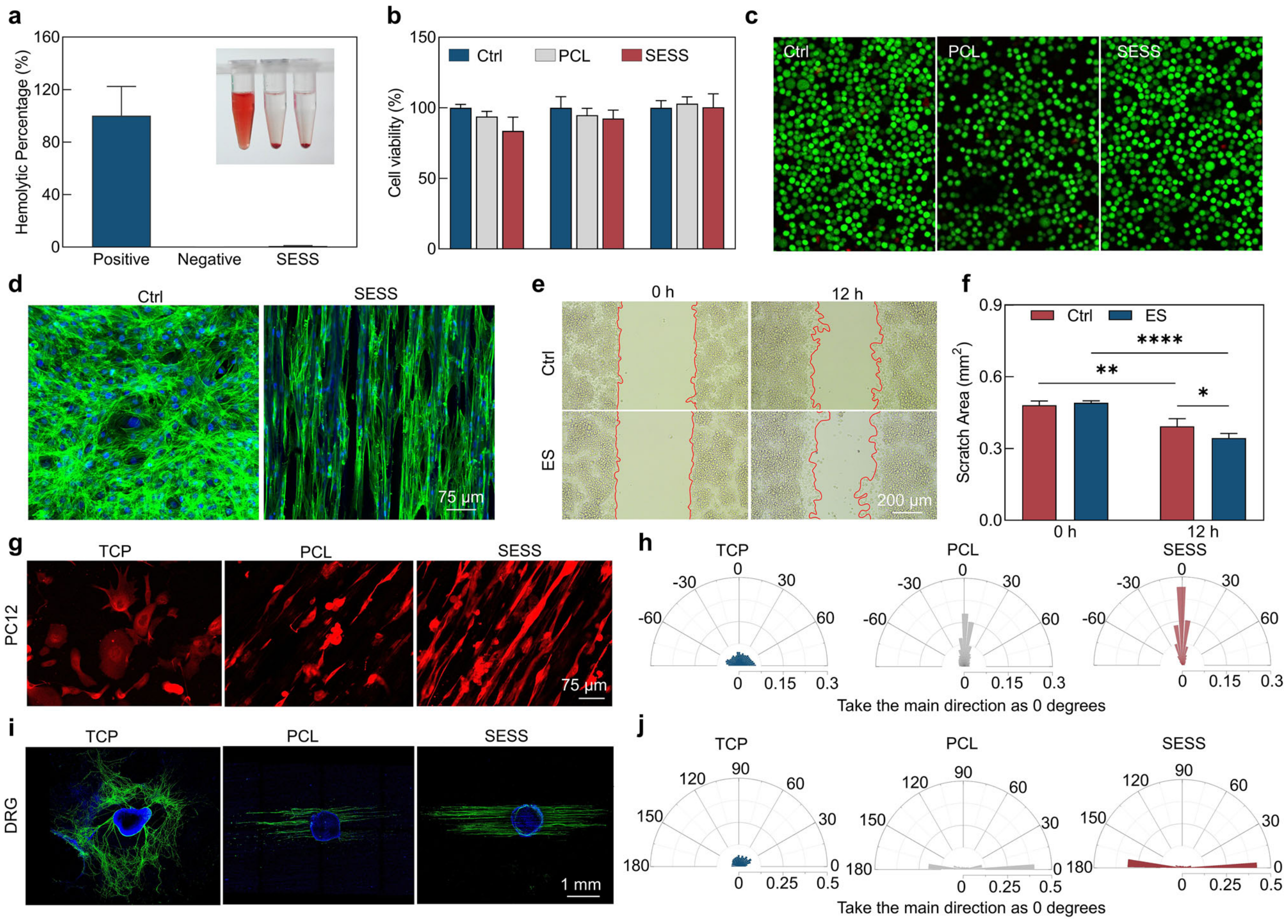

Fig. 3 | Cell compatibility of the SESS scaffold. **a** Hemolysis ratios of the positive control, negative control, and SESS groups (*n* = 3). **b** Percentage of cell viability on PCL and SESS film surfaces at 24, 48, and 72 h, measured by CCK-8 assay, compared with controls (*n* = 5). **c** Live/dead staining of cells. **d** Immunofluorescence staining of the cytoskeleton in MSCs cultured on different substrates. **e** Scratch experiment photo. **f** Quantification of scratch area. **g** Representative images showing the growth of PC12 cells in different experimental groups. **h** Statistical analysis of PC12 cells' growth directionality on different substrates. **i** DRGs cultured on different substrates. **j** Quantitative analysis of axonal elongation direction of DRGs. In **a**, **b** and **f**, data are represented as mean ± SD. In **f**, the statistical significance was determined using two-way ANOVA with Šídák's multiple comparison test, $^{*}P < 0.05$, $^{**}P < 0.01$, $^{****}P < 0.0001$.

nanostructures of SESS, combined with the low-intensity DC stimulation (50 mV), can provide guidance cues to promote directional axonal growth from single cells to tissue explants.

SESS achieves nerve regeneration in rats with a sciatic nerve defect

To evaluate SESS-mediated nerve regeneration via self-powered electrical stimulation in vivo, a rat sciatic nerve defect model was established. SD rats were randomly assigned to five groups: autograft, PCL scaffold, M-SESS (Mg/PCL layer facing the spinal cord), S-SESS (Si layer facing the spinal cord), and Blank (Fig. S11). A 10 mm segment of the sciatic nerve was surgically excised in each rat to establish a critical-size defect model, followed by implantation of either an autologous nerve graft or the corresponding scaffold at the defect site (Fig. 4a). Importantly, the M-SESS and S-SESS groups share identical material composition and degradation behavior but differ only in implantation orientation, constituting a mirror-symmetric deployment that enables decoupling of electrical stimulation direction from degradation-derived biochemical effects.

The self-powered mechanism of SESS is illustrated in Fig. 4b. Upon contact with body fluids, the Mg layer gradually hydrolyzes to release electrons, which migrate toward the Si terminal, thereby generating a stable potential difference across the SESS. The simulated potential distribution (Fig. 4c) further demonstrates that SESS can generate a stable potential distribution under the drive of tissue fluid, providing continuous electrical stimulation for nerve regeneration. Voltage monitoring during scaffold implantation revealed that SESS generated an initial output of approximately 400 mV, measured as the potential difference across the neural tissue at both ends of the scaffold. This value decreased to about 50 mV after 90 days, demonstrating the long-term stable electrical output capability of the scaffold (Fig. 4d). Even at 50 mV, the voltage is still sufficient for therapeutic electrical stimulation, as it remains within the biologically effective range for promoting cellular responses. Because the electrochemical reactions and degradation kinetics are identical in M-SESS and S-SESS, any difference in regenerative outcomes can be attributed to the directionality of the generated electric field rather than material degradation.

Three months after implantation, nerve tissue samples were harvested and immunostained for the mature neuronal marker neurofilament-09 (NF09) and the Schwann cell marker S100. As shown in Fig. 4e and Supplementary Fig. S12, the S-SESS group exhibited much stronger NF09 and S100 expression than the PCL and M-SESS groups, indicating enhanced nerve fiber and Schwann cell regeneration under sustained electrical stimulation. Notably, the expression levels were comparable to those in the autograft group, suggesting similar regenerative efficacy. In contrast, the M-SESS group, despite releasing identical degradation products and producing comparable electrical output magnitude, failed to achieve similar regeneration, underscoring the importance of stimulation polarity.

To examine the quality of regenerated nerves and the level of remyelination, the ultrastructure of the tissues was analyzed using transmission

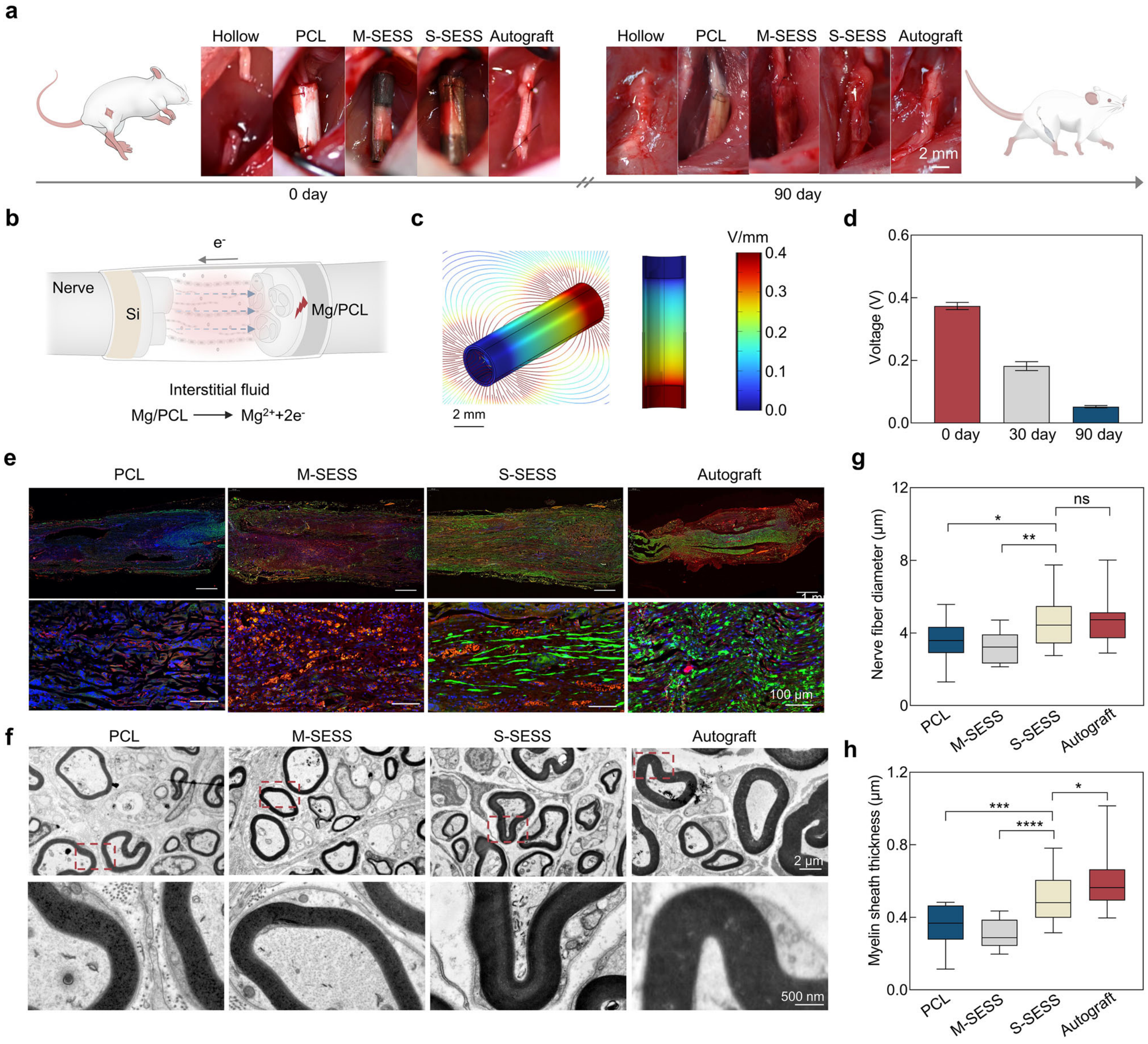

Fig. 4 | The S-SESS successfully achieved in situ nerve repair in rats with PNI. **a** Surgical images of PIN rats before and after different treatments. **b** Schematic illustration of nerve repair with SESS. **c** Simulated electric field distribution of SESS. **d** In vivo output of SESS in PIN rats at different time points. **e** Representative longitudinal immunofluorescence images of regenerated sciatic nerves; red fluorescence indicates NF09, and green fluorescence indicates S100. **f** Representative TEM images showing regenerated myelinated axons in the four experimental groups. **g**, **h** Quantification of nerve fiber diameter and myelin sheath thickness. In **d**, **g** and **h**, data are represented as mean ± SD. In **g** and **h**, the statistical significance was determined using one-way ANOVA with Tukey's multiple comparison test, $^{*}P < 0.05$, $^{**}P < 0.01$, $^{***}P < 0.001$, $^{****}P < 0.0001$.

electron microscopy (TEM). TEM images (Fig. 4f) revealed that the S-SESS group exhibited the largest axonal diameter (4.56 ± 1.34 μm) and the thickest regenerated myelin sheath (0.50 ± 0.12 μm), values comparable to those observed in the autograft group (axonal diameter: 4.61 ± 1.23 μm; myelin thickness: 0.61 ± 0.15 μm) (Fig. 4g, h). In contrast, the axonal diameter and myelin thickness in the PCL group were 3.57 ± 1.19 μm and 0.35 ± 0.12 μm, respectively. Compared to the S-SESS group, the insufficient axonal and myelin regeneration in the PCL group can be attributed to the failure to reproduce endogenous bioelectrical signals. Although the M-SESS group generated electrical signals of similar intensity, its mirror-inverted orientation produced a reverse electric field relative to physiological nerve conduction, leading to regenerative outcomes (axonal diameter: 3.22 ± 0.86 μm; myelin thickness: 0.31 ± 0.08 μm) comparable to the PCL group. These results confirm that the directionality of electrical stimulation, rather than its mere presence, is essential for effective nerve regeneration.

SESS promotes peripheral nerve repair with functional recovery

Peripheral nerve injury not only leads to sensory deficits but is often accompanied by motor dysfunction and distal muscle atrophy, severely compromising patients' quality of life. Therefore, evaluating the efficacy of nerve repair materials requires a comprehensive assessment of multiple parameters, including nociceptive sensitivity, motor function, and muscle condition. In this study, we systematically assessed the regenerative effects of SESS in a rat sciatic nerve defect model through behavioral, electrophysiological, and histological analyses.

First, mechanical threshold testing was performed to compare nociceptive sensitivity among different groups at 1 and 3 months post-injury (Fig. 5a, b). The results showed that the S-SESS group and autograft group exhibited significantly higher pain thresholds than the control, PCL, and M-SESS groups at both time points, indicating superior recovery of nerve conduction and sensory function. Subsequently, gait analysis was conducted to evaluate motor function recovery. According to the formula of the sciatic

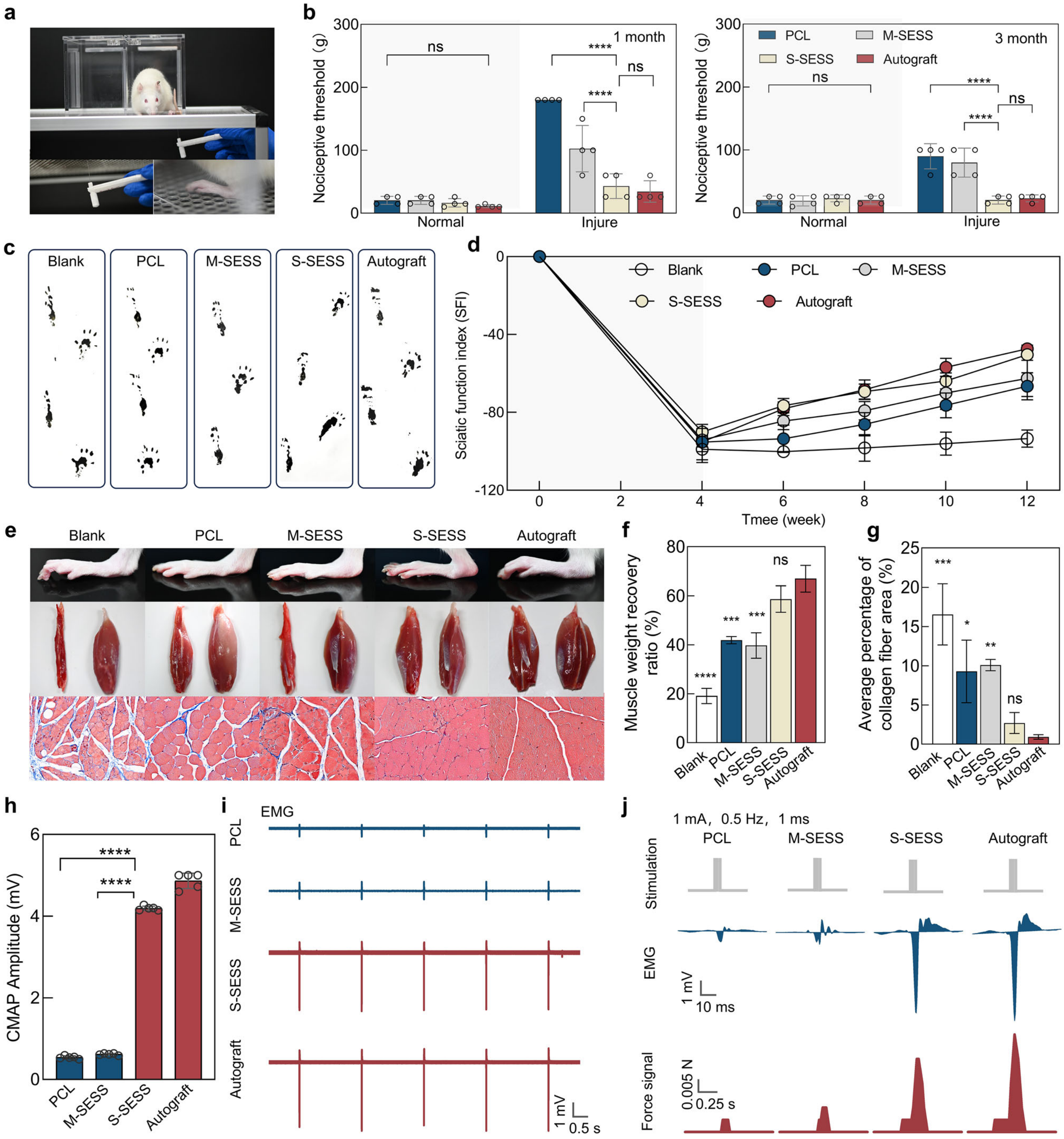

Fig. 5 | The S-SESS effectively restored nerve conduction and motor function in rats with PNI. **a** Representative von Frey test images of rats in different experimental groups. **b** Mechanical assessment of nociceptive withdrawal thresholds of ipsilateral and contralateral hind paws after nerve injury, evaluated by the von Frey test in the PCL scaffold group, autograft group, M-SESS group, and S-SESS group at 1 and 3 months post-surgery. **c** Representative footprint images of rats after treatment in different experimental groups. **d** SFI curves of different experimental groups at 4, 6, 8, 10, and 12 weeks. **e** Representative images of rat hind paws and gastrocnemius muscles, as well as Masson's trichrome staining of gastrocnemius muscles in each group. **f** Statistical analysis of the percentage of muscle weight ratio between the ipsilateral and contralateral legs in each group. **g** Quantitative analysis of the average collagen fiber area percentage in each group. **h** Statistical analysis of the average CMAP amplitudes in different experimental groups ($n = 5$). **i** Representative CMAP waveforms of different experimental groups at 12 weeks. **j** CMAP and force signals generated by the hind paws of rats under electrical stimulation in different experimental groups. In **b**, **d**, **f**, **g** and **h**, data are represented as mean ± SD. In **b**, the statistical significance was determined using two-way ANOVA with Tukey's multiple comparison test, $****P < 0.0001$. In **f**, **g** and **h**, the statistical significance was determined using one-way ANOVA with Tukey's multiple comparison test, $*P < 0.05$, $**P < 0.01$, $***P < 0.001$, $****P < 0.0001$.

functional index (SFI), its value was related to the footprint length (PL), toe span (TS), and middle toe span (IT) as shown in Fig. S13a. When PL and IT are each similar across groups, the larger TS meant the lower absolute SFI values. From Fig. 5c and S13b-c, the TS in the S-SESS group and autograft group were larger than other groups indicated the better recovery of nerve conduction and sensory function. Furthermore, we calculated the values of SFI in different groups at different time points using the formula. At 3 months post-repair, SFI of S-SESS-treated rats (−50.38 ± 1.41) approached that of the autograft group (−47.37 ± 1.89), with a significantly faster motor recovery compared to other groups (Blank group: −93.46 ± 4.40, PCL group: −66.59 ± 6.95, M-SESS group: −62.51 ± 9.30) (Fig. 5d). The S-SESS group with lower absolute SFI values indicates better nerve regeneration compared with blank group, PCL group, and M-SESS group. What's more, observation of the operated hindlimb at 3 months post-surgery revealed that toe morphology in the S-SESS group closely resembled that of the autograft group, with intact toes, whereas the Blank, PCL, and M-SESS groups exhibited varying degrees of toe autophagy (Fig. 5e).

Sciatic nerve injury profoundly affects the physiological state of innervated muscles, further compromising motor function. To evaluate the effect of SESS on muscle recovery and neuromuscular conduction, we assessed muscle morphology, weight, and electrophysiological parameters. The control and PCL groups exhibited severe muscle atrophy, while the S-SESS and autograft groups maintained preserved muscle morphology, with HE staining showing intact myofiber architecture. Quantitative analysis demonstrated that muscle weight recovery in the S-SESS group (58.69 ± 5.40%%) was significantly higher than in the control (19.09 ± 3.10%) and PCL (41.91 ± 1.50%) groups, approaching the autograft group (66.99 ± 5.41%) (Fig. 5f). Collagen deposition analysis (Fig. 5g) revealed that the S-SESS group exhibited significantly lower collagen content (2.69 ± 1.33%) than the PCL (9.28 ± 3.99%) and M-SESS (10.08 ± 0.71%) groups, indicating that S-SESS promoted muscle recovery.

Electrophysiological assessment revealed similar trends. The PCL and M-SESS groups exhibited low compound muscle action potential (CMAP) amplitudes of 0.54 ± 0.04 mV and 0.62 ± 0.02 mV, respectively. Whereas the S-SESS (4.19 ± 0.05 mV) and autograft (4.87 ± 0.19 mV) groups generated high-amplitude CMAP signals with no significant difference (Fig. 5h, i). Upon electrical stimulation of the sciatic nerve, S-SESS and autograft groups elicited clear electromyographic activity and robust muscle contraction, whereas the PCL and M-SESS groups showed minimal responses (Fig. 6j). Bilateral conduction tests using proximal/distal reciprocal stimulation revealed that stable, high-amplitude evoked potentials in both stimulation directions for S-SESS and autograft groups, in contrast to weak or unstable responses in PCL and M-SESS groups (Fig. S14). Collectively, these results indicate that S-SESS not only promotes axonal bridging and functional connectivity but also reestablishes a functional neuromuscular loop capable of driving muscle contraction.

Integrating morphological and behavioral results, the diode characteristics of S-SESS and the directional electric field generated by tissue-fluid-driven currents underlie its ability to facilitate high-quality functional regeneration. Although both S-SESS and M-SESS provide unidirectional electrical stimulation, their efficacy differs significantly, primarily due to alignment with physiological nerve signal propagation. S-SESS directs current from the spinal side to the distal nerve, consistent with the natural action potential flow, forming a stable electric field that guides axonal extension and synapse formation. In contrast, M-SESS conducts current in the opposite direction (distal → proximal), generating reverse-field interference that reduces axonal guidance efficiency and delays functional recovery. This difference in efficacy underscores that the alignment of electrical stimulation direction with natural nerve signal propagation is crucial, as demonstrated by the superior regenerative effects of S-SESS over M-SESS. These findings highlight that proper alignment of stimulation direction with endogenous nerve signal propagation is critical for optimizing axonal regeneration and neuromuscular functional restoration.

Molecular mechanisms of SESS in repairing PNI

Transcriptome sequencing was conducted on regenerating nerve tissues from the Autograft (AG), Blank, and SESS groups to investigate the molecular mechanisms underlying SESS-mediated nerve repair. Differentially expressed genes (DEGs) analysis revealed distinct gene sets among the groups, as shown in the upset plot (Fig. 6a). The heatmap of DEGs (Fig. 6b) indicated that, compared with the blank group, the SESS group exhibited the greatest differences, but the smallest difference compared to the AG group (Fig. S15), suggesting that SESS achieved a therapeutic effect similar to that of the autograft.

Kyoto encyclopedia of genes and genomes (KEGG) and gene ontology (GO) enrichment analyses were conducted on DEGs between the SESS and Blank groups (Fig. 6c, d). KEGG analysis showed that the DEGs were significantly enriched in neural repair–related pathways, including cell adhesion molecules, PI3K-Akt, calcium, Rap1 signaling, axon guidance, and ECM–receptor interaction (Fig. 6c). GO enrichment analysis revealed that terms associated with neural repair, such as regulation of axon extension, response to axon injury, axonogenesis, axon development, axon regeneration, axon extension, were also highly enriched (Fig. 6d). Figure 6e further illustrates the key genes involved in these major KEGG pathways. Many genes participate in multiple nerve repair-related pathways, suggesting they may play important roles in axonal growth, cell adhesion, and signal transduction (Fig. S16).

The heatmap and volcano plot of the DEGs (Fig. 6f, g) showed that, compared to the blank group, the SESS group had 2059 upregulated and 2352 downregulated genes (Fig. 6g). Among the upregulated genes, Itgb2, Itga4, Itgal, and Sdc1 were associated with cell adhesion; Camk1, Camk2d, and Cacna1i were related to calcium channels; and Angpt1, Bdnf, Map2k1, Grb2, Csf1, and Rap1b were involved in the PI3K-Akt and Rap1 signaling pathways. Upregulation of S100a4 and S100a11, genes related to myelination, was also observed. Additionally, anti-inflammatory genes Tgfb1, Tgfbr1, and Il10 were upregulated, while pro-inflammatory genes Il17rb, Il17re, Il17rd, Il17rc, and Ager were downregulated.

Finally, we constructed a Protein-Protein Interaction (PPI) network using the DEGs between the SESS and Blank groups (Fig. 6h). Genes upregulated in the SESS group and associated with neural repair are marked in red. In this network, larger red nodes indicate genes with greater importance. The PPI network analysis suggests that these neural repair–related genes may play key roles in mediating processes such as axonal growth, myelination, and cell adhesion during peripheral nerve regeneration.

These results collectively demonstrate that SESS promotes the repair of peripheral nerve injury by modulating multiple genes and signaling pathways, including those involved in calcium channels, enhancing cell adhesion, PI3K–Akt signaling pathway, and inflammatory regulation thereby creating an environment conducive to functional nerve regeneration.

Discussion

In summary, we have developed a fully biodegradable Si–Mg galvanic cell-based symbiotic electrical stimulation scaffold (SESS) capable of generating month-long, adaptive electrical stimulation driven by tissue fluids in vivo while consuming ROS. By integrating semiconductor silicon with bioresorbable metals and a soft fibrous matrix, SESS achieves stable electrical output, mechanical compliance with dynamic tissues, and complete degradation without secondary surgery. Using a rat sciatic nerve defect model, we demonstrated that SESS provides regenerative outcomes comparable to autologous nerve grafts. Importantly, mirror-symmetric implantation enabled decoupling of electrical stimulation effects from degradation products, unambiguously confirming the therapeutic role of directed electrical cues. This work establishes a versatile galvanic bioelectronics strategy for self-powered, transient implants and offers new design principles for next-generation regenerative bioelectronic systems.

Methods

Materials

PCL (6500) was purchased from Jinan Daigang Biomaterial. Dichloromethane (DCM, 99.8%) was supplied by Macklin. Mg particles were purchased from Beijing Deke Daojin Science and Technology Co., Ltd. (30 μm). The recombinant human β-NGF was purchased from Thermo Fisher Scientific. The 4% Paraformaldehyde (PFA) and Triton X-100 were purchased from Beyotime Biotechnology. The Calcein-AM/PI live/dead cell double stain kit, RPMI 1640 essential medium, DMEM essential medium, fibronectin, and goat serum were obtained from Solarbio. The anti-NF200 antibody, phalloidin-iFluor 555 Reagent, anti-GFAP antibody, anti-beta III tubulin antibody, and anti-S100 beta antibody were obtained from Abcam.

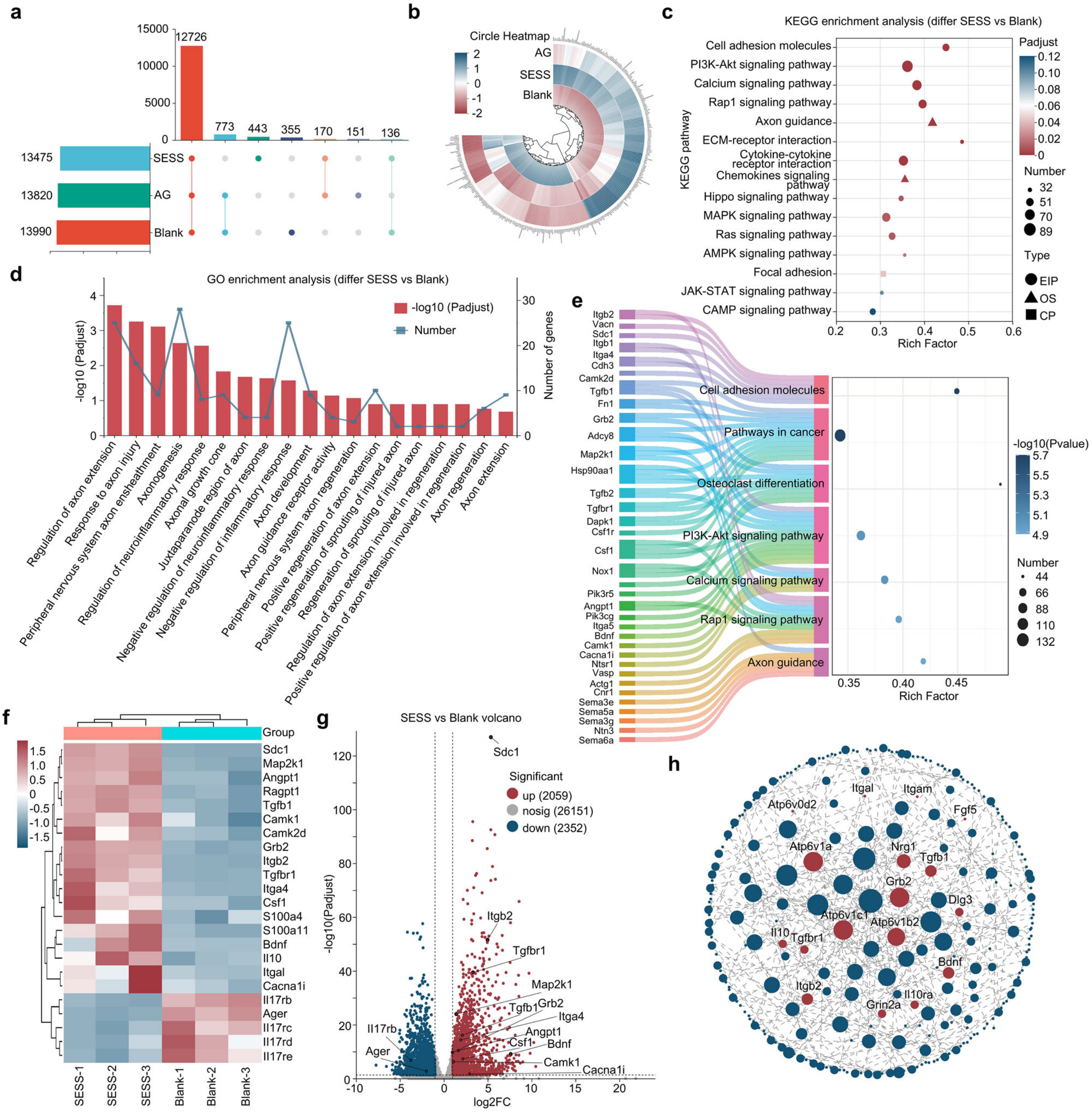

Fig. 6 | Molecular mechanism by which the SESS repairs the injured sciatic nerve in rats was determined based on transcriptomic analysis. a Upset plot of differentially expressed genes between groups. **b** Circos heatmaps showing differential gene expression between the different groups. **c** Bubble plots of KEGG pathways enriched in the differentially expressed genes in the SESS group relative to the Blank group. **d** The line and bar chart of GO pathways enriched in the differentially expressed genes in the SESS group relative to the Blank group. **e** Pathway enrichment analysis of differentially expressed genes in the highlighted cluster based on the KEGG database. **f** Heatmap of differentially expressed genes related to nerve repair between the SESS and Blank groups. **g** Volcano maps of differential expression genes in the SESS group relative to the Blank group. **h** The String interaction network depicts differentially expressed genes between the SESS and Blank groups. Genes related to nerve repair are highlighted with red dots.

Goat anti-rabbit IgG (Alexa Fluor 488) and goat anti-mouse IgG H&L (Alexa Fluor 647) were purchased from Proteintech.

Preparation of SESS

Polycaprolactone (PCL) was dissolved in dichloromethane at a concentration of 15 wt% and stirred for 6 h to obtain a homogeneous solution. Random PCL nanofiber membranes were fabricated via electrospinning using a 10 mL syringe (23 G needle) at a flow rate of 1.5 mL/h, with a needle-to-collector distance of 10 cm. The collector reciprocated over a 10 cm range at a speed of 10 cm/min and rotated at 300 rpm. A voltage of +7 kV/−3 kV was applied for 60 min. For the preparation of aligned PCL fibers, the collector rotational speed was increased to 2500 rpm, and the reciprocation speed was reduced to 1 cm/min, enabling fiber alignment along the rotational direction (120 min). All membranes were vacuum-dried overnight at room temperature to remove residual solvent.

A patterned mask was fabricated on 1 mm thick acrylic using laser cutting for later metal deposition. To enhance metal adhesion, the PCL membranes underwent plasma treatment to improve surface activity and hydrophilicity. Mo, Mg, and Si were deposited using a magnetron sputtering system (Denton, Discovery 635, USA). Specifically, Mo was sputtered through a shadow mask at 100 W for 60 min, Mg was sputtered through a shadow mask at 100 W for 60 min, and Si was deposited through a shadow mask using radio frequency sputtering at 150 W for 120 min. Mg powder (30 μm) was incorporated into a 15% PCL solution at a mass ratio of 2:1, followed by casting into molds and solvent evaporation to obtain Mg/PCL composite films. The films were then cut into predefined dimensions and thermally pressed onto one end of the scaffold electrode for fixation.

Characterization measurements

The nanofibers' microstructure and elemental composition were characterized by a Nova 450 SEM with a Raith/EDAX EDS system. The voltage and current of the nerve scaffold were measured using an electrometer (Keithley 6517B) and an oscilloscope (LeCroy, HDO6104). Stress–strain curves were measured using an ESM301/Mark-10 system, and current–voltage (I–V) characteristics were recorded with a semiconductor parameter analyzer (Keithley 4200).

ROS scavenging assay

The ROS scavenging experiment was conducted using the Fe^{2+}/H_2O_2 Fenton reaction. In the blank group, 20 μL of 10 mM $FeSO_4$ was added to 2 mL of 5 mM H_2O_2 and allowed to react for 1, 2, or 3 min. In the SESS group, SESS was added under the same conditions and reacted for the same durations. Subsequently, 40 μL of 1 mM methyl violet was added to each sample, and after 2 min of reaction, the absorption spectrum was measured to evaluate the ROS scavenging capability of SESS.

Cell proliferation and viability (CCK-8)

HaCaT cells were used to evaluate the cytocompatibility of the samples. PCL and SESS were cut into 3 cm^2 pieces, sterilized under UV light, immersed in 75% ethanol for 3 min, and rinsed thrice with PBS. The sterilized samples were then immersed in 1 mL of complete culture medium and incubated at 37 °C for 24 h to obtain the extract solutions. HaCaT cells were seeded in 96-well plates and cultured with the corresponding material extract solutions, while cells cultured in fresh complete medium served as the control group. Cell viability on days 1, 2, and 3 was determined by the CCK-8 assay, measuring absorbance at 450 nm.

Live/Dead Cell Staining

For fluorescence staining, the preparation of material extract solutions was the same as described in the CCK-8 assay. HaCaT cells were cultured with the material extract solutions for 24 h. After incubation, cells were detached with trypsin, centrifuged, and resuspended in Calcein-AM staining solution. The cell suspension was incubated at 37 °C for 25 min in the dark, followed by the addition of propidium iodide (PI) staining solution and incubation for an additional 5 min at room temperature in the dark. Cells were collected by centrifugation (450×g, 5 min), washed with 1× PBS, resuspended, and observed under a confocal laser scanning microscope; live cells appeared green and dead cells red.

Cell migration

Scratch assay plugin was used to assess the cell migration ability. In total, 80 μL Rat Schwann cells (RSC96) with a density of 5×10^5 cells mL^{-1} were seed in the plugin in a 24-well plate. After 24 h, when cell growth is observed to have reached 100% confluency, gently removed the insert and added fresh medium to continue normal culture. After 12 h of DC electrical stimulation at 50 mV (Simulate the output of SESS) via a signal generator, observe cell migration under a microscope and quantify the scratch area.

PC12 cell axon outgrowth

The PC12 cells were seeded with a density of 5×10^3 cells mL^{-1} on the TCP, PCL, and SESS in a 24-well plate. After 24 h of incubation, the culture medium was replaced with the medium containing 50 ng mL^{-1} NGF. After culturing for 7 days, Cells were fixed, labeled with the neuronal marker Tuj1, and imaged by confocal microscopy to assess morphology and axonal growth.

DRG explant culture and growth assessment

Dorsal root ganglia (DRGs) were isolated from neonatal rats at postnatal day 3. The ganglia were dissected alongside the spinal column, and distal nerve endings were trimmed. DRG explants were then seeded on TCP, PCL, and SESS substrates (pretreated with rat tail tendon type I collagen) and cultured for 7 days. The explants and associated cells were fixed, immunostained with the neuronal marker Tuj1, and imaged by confocal microscopy.

Hemolytic test

Fresh blood (1 mL) was collected from 6-week-old male rats (200 g) into anticoagulant tubes. Red blood cells were washed with PBS and resuspended to prepare a blood working solution. For the test group, 200 μL of this solution was mixed with 800 μL of SESS leachate (1 mg/mL, prepared by incubating SESS in saline for 3 days). Positive and negative controls were prepared by mixing the blood solution with water or PBS, respectively. Samples were incubated at 37 °C for 4 h, then centrifuged and photographed, with the absorbance of the resulting supernatant measured at 577 nm.

Animal surgery and treatment

All animal studies were carried out under the approval of the Ethics Committee of the Chinese Academy of Sciences (202403042). A total of 30 adult female SD rats (200–250 g) were randomly divided into five groups: Blank, Autograft, PCL, SESS-M, and SESS-S. Rats were anesthetized with pentobarbital sodium, and the right sciatic nerve was exposed following standard skin preparation and disinfection. The peripheral nerve was transected to produce a 10-mm defect in its midsection. In the stent implantation group, 1 mm of each nerve stump was placed into the stent and fixed with 9-0 sutures. For the autograft group, the nerve tissue causing the defect segment will be sutured back to the defect site using 9-0 suture thread. During the first 3 days after surgery, rats were given a certain amount of penicillin to prevent postoperative infection.

Measurement of mechanical nociception using von Frey tests

SD rats were placed individually in a transparent chamber with a metal mesh floor and allowed to habituate for 30 min. Mechanical sensitivity was assessed using a series of seven calibrated von Frey filaments (10-200 g) applied to the plantar surface of the ipsilateral or contralateral hind paw. Each filament was tested 10 times, and the force inducing ≥6 withdrawals was taken as the nociceptive threshold, capped at 200 g.

Gait analysis experiment

The recovery of motor function in rats was evaluated using the imprinting method at 4,6, 8, 10, and 12 weeks postoperatively. Apply non-toxic dyes of different colors to the front and back feet of rats, and let them walk on white paper, leaving footprints. Rat motor ability was evaluated via the sciatic nerve function index (SFI), derived from stride length, step width, and step frequency.

The sciatic nerve function index (SFI) is an indicator of motor nerve dysfunction, and the score is calculated using the following formula:

$$\begin{aligned} SFI = & -38.3\,(EPL - NPL)\,NPL + 109.5\,(ETS - NTS)\,NTS \\ & +13.3\,(EIT - NIT)\,NIT - 8.8 \end{aligned} \tag{1}$$

Among them, NPL represents normal footprint length, NTS represents normal toe span, NIT represents normal middle toe span, EPL represents experimental footprint length, ETS represents experimental toe, and EIT represents experimental middle toe span.

EMG testing experiment

Prior to tissue collection (3-month repair period), SD rats were deeply anesthetized with sodium pentobarbital. Surrounding connective tissue was carefully separated to expose the sciatic nerve while preserving muscle integrity. During the experiment, the injured site of the nerve was identified, with the end proximal to the spinal cord defined as the upper end and the distal end defined as the lower end. A stimulating cuff electrode (Kedou BC) was placed at the upper end of the nerve to deliver electrical stimulation (1 Hz frequency, 100 μA current, 1 ms pulse width; STG 4008 stimulator, MCS Stimulus Generators), thereby evoking compound muscle action potentials. A recording electrode (Kedou BC) was positioned at the lower end, and neural signals were acquired using an electrophysiological recording system (BLACKROCK). In the reverse setup, the recording electrode was placed at the upper end while the stimulating electrode was positioned at the lower end, and the same stimulation and recording procedures were performed.

Evaluation of Hindlimb Motor Function Induced by Nerve Stimulation

At 12 weeks post-surgery, all rats underwent functional testing. Under light isoflurane anesthesia (1.5%), the animals were placed prone, and both sciatic nerves were exposed. A cuff electrode was placed around the sciatic nerve, and monophasic square-wave pulses (1 Hz frequency, 100 μA current, 1 ms pulse width) were delivered using a stimulator (STG 4008 stimulator, MCS Stimulus Generators). The plantar surface of the tested hindlimb was kept in contact with a force transducer (Mark-10). For each stimulation sequence, the peak kicking force, defined as the maximum force (mN) generated during a single contraction, was analyzed and recorded.

Morphology of muscle

At 12 weeks after surgery, the rats were euthanized, and immediately the bilateral gastrocnemius muscles of each group were isolated and recorded for wet weight. Muscle tissues were fixed in formalin, paraffin-embedded, sectioned, and stained with Masson trichrome. Sections were imaged by light microscopy, and blue collagen areas were quantified in ImageJ using at least three random regions per slice.

Morphology of the sciatic nerve

At 12 weeks, sciatic nerves were harvested, fixed in 10% formalin overnight, dehydrated, and paraffin-embedded for 4 μm sectioning. Sections were blocked with 0.3% Triton X-100, 3% BSA, and 10% FBS for 2 h, incubated overnight with mouse anti-neurofilament (NF09, 1:200) and rabbit anti-S100 (1:200) antibodies, and then treated with Alexa Fluor-conjugated secondary antibodies for 1 h. Sections were scanned (P250 Flash, 3DHISTECH), and three random regions per sample were analyzed. For ultrastructural analysis, rats were perfusion-fixed with saline, 4% PFA, and 2.5% glutaraldehyde. Sciatic nerves were fixed in 2.5% glutaraldehyde, post-fixed in 1% osmium tetroxide, dehydrated, and embedded in epoxy resin. Ultra-thin sections were stained with uranyl acetate and lead citrate, and myelin sheaths of regenerated nerves were examined by transmission electron microscopy (Tecnai G2 F20, FEI, Czech). ImageJ was used to measure axon diameters and myelin thickness, with at least 20 myelin sheaths analyzed per group.

Reporting summary. Further information on research design is available in the Nature Research Reporting Summary linked to this article.

Statistical analysis

Statistical analyses were statistically analyzed with GraphPad Prism 10.0 software, ImageJ software and Origin software program, and all the results were reported as means SD. Significance difference was calculated by one-way ANOVA with Tukey's multiple comparison test, two-way ANOVA with Tukey's multiple comparison test and two-way ANOVA with Šídák's multiple comparison test. Statistical differences were shown with four significance levels ($^{*}p < 0.05$, $^{**}p < 0.01$, $^{***}p < 0.001$, $^{****}p < 0.0001$).

Data availability

All data are available in the main text or the Supplementary Materials. All data needed to evaluate the conclusions in the paper are present in the paper and/or the Supplementary Materials.

Received: 13 January 2026; Accepted: 23 March 2026;

References

1. Shan, Y. et al. A neurodevelopment-inspired self-evolving scaffold for nerve regeneration. *Cell Biomater.* **1**, 100006 (2025).
2. Wang, E. et al. Symbiotic biodegradable flexible supercapacitor in vivo. *Device* **3**, 100724 (2025).
3. Chen, P. et al. Wirelessly powered electrical-stimulation based on biodegradable 3D piezoelectric scaffolds promotes the spinal cord injury repair. *ACS Nano* **16**, 16513–16528 (2022).
4. Chai, M., Li, Y., Li, Y., Zuo, Y. & Li, J. Effect of electrical stimulation generated by self-powered systems for tissue repair. *Acta Biomater.* **201**, 1–33 (2025).
5. Jin, F. et al. Physiologically self-regulated, fully implantable, battery-free system for peripheral nerve restoration. *Adv. Mater.* **33**, 2104175 (2021).
6. Li, L. et al. Implantable zinc–oxygen battery for in situ electrical stimulation-promoted neural regeneration. *Adv. Mater.* **35**, 2302997 (2023).
7. Liu, Z., Wan, X., Wang, Z. L. & Li, L. Electroactive biomaterials and systems for cell fate determination and tissue regeneration: design and applications. *Adv. Mater.* **33**, 2007429 (2021).
8. Kaveti, R. et al. Water-powered, electronics-free dressings that electrically stimulate wounds for rapid wound closure. *Sci. Adv.* **10**, eado7538 (2024).
9. Wang, T. et al. Rehabilitation exercise–driven symbiotic electrical stimulation system accelerating bone regeneration. *Sci. Adv.* **10**, eadi6799 (2024).
10. Liu, Y. et al. Biomimetic electroactive materials and devices for regenerative engineering. *Nat. Rev. Electr. Eng.* **2**, 188–204 (2025).
11. Yuk, H., Wu, J. & Zhao, X. Hydrogel interfaces for merging humans and machines. *Nat. Rev. Mater.* **7**, 935–952 (2022).
12. Shen, J. et al. Mechano-bioactive hydrogel bioelectronics for mechanical-electrical-bioenergetic conversion and glia-modulating neural regeneration. *Nat. Commun.* **16**, 11582 (2025).
13. Yang, D. et al. Synthesis and assembly strategy of electroactive biomaterials and systems for soft tissue engineering applications. *Chemistry* **11**, 102596 (2025).
14. Chen, X. et al. Decellularized extracellular matrix bio-patch with strong and biodegradable wet adhesive interface for sutureless soft tissue defect repair. *J. Nanobiotechnol.* **23**, 673 (2025).
15. Lee, D.-M. et al. An on-demand bioresorbable neurostimulator. *Nat. Commun.* **14**, 7315 (2023).
16. Zhou, M. et al. Contact separation triboelectric nanogenerator based neural interfacing for effective sciatic nerve restoration. *Adv. Funct. Mater.* **32**, 2200269 (2022).
17. Ma, Y., Wang, H., Wang, Q., Cao, X. & Gao, H. Piezoelectric conduit combined with multi-channel conductive scaffold for peripheral nerve regeneration. *Chem. Eng. J.* **452**, 139424 (2023).
18. Chen, G. et al. Biodegradable piezoelectric amino acid nerve guidance conduit repairs long-gap nerve defect under low frequency vibration from massage gun. *Adv. Funct. Mater.* **36**, e10947 (2026).
19. Wu, P. et al. Ultrasound-driven in vivo electrical stimulation based on biodegradable piezoelectric nanogenerators for enhancing and monitoring the nerve tissue repair. *Nano Energy* **102**, 107707 (2022).
20. Choi, Y. S. et al. Stretchable, dynamic covalent polymers for soft, long-lived bioresorbable electronic stimulators designed to facilitate neuromuscular regeneration. *Nat. Commun.* **11**, 5990 (2020).
21. Ahn, H.-Y. et al. Bioresorbable, wireless dual stimulator for peripheral nerve regeneration. *Nat. Commun.* **16**, 4752 (2025).
22. Li, Y. et al. Ultra-low frequency magnetic energy focusing for highly effective wireless powering of deep-tissue implantable electronic devices. *Natl. Sci. Rev.* **11**, nwae062 (2024).

23. Liu, S. et al. Magnetic field-assisted conductive nerve guidance conduit enabling peripheral nerve regeneration with wireless electrical stimulation. *Adv. Funct. Mater.* **35**, 2416548 (2025).
24. Wang, Q., Wang, H., Ma, Y., Cao, X. & Gao, H. Effects of electroactive materials on nerve cell behaviors and applications in peripheral nerve repair. *Biomater. Sci.* **10**, 6061–6076 (2022).
25. Ni, L.M. et al. Electrical stimulation therapy for peripheral nerve injury. *Front. Neurol* **14**, 1081458 (2023).
26. Gordon, T. Electrical stimulation to enhance axon regeneration after peripheral nerve injuries in animal models and humans. *Neurotherapeutics* **13**, 295–310 (2016).
27. Wang, L. et al. A fully biodegradable and self-electrified device for neuroregenerative medicine. *Sci. Adv.* **6**, eabc6686 (2020).
28. Wang, L. et al. A biodegradable and restorative peripheral neural interface for the interrogation of neuropathic injuries. *Nat. Commun.* **16**, 1716 (2025).
29. Qi, F. et al. A self-powered nerve conduit based on zinc-oxygen battery accelerates nerve cell growth. *Colloids Surf. A* **721**, 137225 (2025).
30. Scheib, J. & Höke, A. Advances in peripheral nerve regeneration. *Nat. Rev. Neurol.* **9**, 668–676 (2013).
31. Avraham, O. et al. Profiling sensory neuron microenvironment after peripheral and central axon injury reveals key pathways for neural repair. *eLife* **10**, e68457 (2021).
32. Chen, B., Xiao, Z., Zhao, Y. & Dai, J. Functional biomaterial-based regenerative microenvironment for spinal cord injury repair. *Natl. Sci. Rev.* **4**, 530–532 (2017).
33. Smith, D. H. et al. Tissue-engineered grafts exploit axon-facilitated axon regeneration and pathway protection to enable recovery after 5-cm nerve defects in pigs. *Sci. Adv.* **8**, eabm3291 (2022).
34. Jessen, K.R. & Mirsky, R. The success and failure of the Schwann cell response to nerve injury. *Front. Cell. Neurosci.* **13**, 33 (2019).
35. Cattin, A. L. et al. Macrophage-induced blood vessels guide Schwann cell-mediated regeneration of peripheral nerves. *Cell* **162**, 1127–1139 (2015).
36. Hilton, B. J., Griffin, J. M., Fawcett, J. W. & Bradke, F. Neuronal maturation and axon regeneration: unfixing circuitry to enable repair. *Nat. Rev. Neurosci.* **25**, 649–667 (2024).
37. Zhang, H. et al. Mechanically robust neuroprotective stent by sequential Mg ions release for ischemic stroke therapy. *Nat. Commun.* **16**, 6557 (2025).
38. Yao, Z. et al. Bioactive MgO/MgCO3/polycaprolactone multi-gradient fibers facilitate peripheral nerve regeneration by regulating Schwann cell function and activating wingless/integrase-1 signaling. *Adv. Fiber Mater.* **7**, 315–337 (2025).
39. Cai, Y.Q. et al. The GDNF-gel/HA-Mg conduit promotes the repair of peripheral nerve defects by regulating PPAR-g/RhoA/ROCK signaling pathway. *iScience.* **27**, 108969 (2024).
40. Kim, H. et al. Controlled magnesium ion delivery via Mg-sputtered nerve conduit for enhancing peripheral nerve regeneration. *Adv. Healthc. Mater.* **14**, 2500063 (2025).
41. Huang, Y. et al. Bioelectronics for electrical stimulation: materials, devices and biomedical applications. *Chem. Soc. Rev.* **53**, 8632–8712 (2024).
42. Yang, Y. et al. Engineering a wirelessly self-powered and electroconductive scaffold to promote peripheral nerve regeneration. *Nano Energy* **107**, 108145 (2023).

Acknowledgements

The authors acknowledge the funding support from the National Natural Science Foundation of China grants 52373256(to H.O.), T2125003 (to Z.L.), 82322037 (to H. F.) and 62004010 (to H.O.); Youth Innovation Promotion Association CAS grant 2023176 (to H.O.); Beijing Natural Science Foundation grants 7232347 (to H.O.), 7264408 (to E.W.), Z240022 (to Z.L.) and L245015 (to Z.L.); Beijing Nova Program grant 2024047 (to H.O.), 20240484655 (to Z.L.); Fundamental Research Funds for the Central Universities grant E2E45101X2 (to H.O.). The authors appreciate the members of the University of Chinese Academy of Sciences research facilities for their help in microfabrication/characterization.

Author contributions

E.G.W., J.H., and Y.Z.S. contributed equally to this work. H.O., Z.L., and L.L.X. conceived and coordinated the project and experiments. E.G.W., J.H., L.L.X., D.J.J, B.J.S., X.W., and H.Q.F. assisted in sample preparation, concept development. E.G.W., L.L., C.Z., Y.C.Q., and X.W. conducted the material preparation and characterization. E.G.W., Y.B., and X.W. conducted the electrical test. J.H., Y.Z.S, X.C., X.Z.W., and L.L.X. conducted the cell experiment. E.G.W., J. H., Y.Z.S, L.L.X., and Y.F.R. conducted the in vivo experiments in SD rats. E.G.W., L.L.X., and H.O. prepared the paper. H.O., Z.L., L.L.X., and H.Q.F. directed the project. All authors read and approved the paper.

Competing interests

The authors declare no competing interests.

Additional information

Supplementary information The online version contains supplementary material available at https://doi.org/10.1038/s41528-026-00574-0.

Correspondence and requests for materials should be addressed to Hongqing Feng, Lingling Xu, Zhou Li or Han Ouyang.

Reprints and permissions information is available at http://www.nature.com/reprints